Project Title:	MIRACLE - Microscopic Image Processing Analysis Coding and Modelling Environment
Contract No:	PIRSES-GA-2009-247091
Instrument:	SESAM
Thematic Priority:	Medical image processing
Start of project:	1 May 2010
Duration:	46 months

Deliverable No: D6/26

Workshop Organization II

Due date of deliverable:	15 September 2013
Actual submission date:	24 October 2013
Version:	1
Main Authors:	Alican Bozkurt, A. Enis Cetin

Project ref. number	PIRSES-247091
Project title	MIRACLE - Microscopic Image Processing Analysis Coding and Modelling Environment

Deliverable title	Workshop Organization II
Deliverable number	D6-26
Deliverable version	V1
Previous version(s)	-
Contractual date of delivery	15 September 2013
Actual date of delivery	24 October 2013
Deliverable filename	Miracle D6-26 Workshop Organization II.docx
Nature of deliverable	Report
Dissemination level	Public
Number of pages	12
Workpackage	6
Partner responsible	BILKENT
Author(s)	Alican Bozkurt
Editor	A. Enis Cetin
EC Project Officer	Alexandra Pedersen

Abstract	2nd MIRACLE Workshop has been organized as a part of MUSCLE International Workshop on Computational Intelligence for Multimedia Understanding, 3-4 October 2013, in Dedeman Antalya Hotel and Convention Center, Antalya Turkey. The Workshop had 22 presentations, 4 of whom are from MIRACLE Workshop.
Keywords	Workshop

Introduction

2nd MIRACLE Workshop was organized as a part of MUSCLE International Workshop on Computational Intelligence for Multimedia Understanding, 3-4 October 2013, in Dedeman Antalya Hotel and Convention Center, Antalya Turkey. Two sessions consisting of four papers and an invited presentation by Prof. Metin Gurcan of Ohio State University are presented during the Workshop. 28 scientists attended the meeting as shown in Figure 1.


Figure 1 Audience

Workshop technical program is given below in Table 1.

One of the plenary talks of the MUSCLE meeting was given by Dr. Metin Gurcan with title "Medical Image Analysis: Visual Decomposition and Modeling".

The following presented papers will appear in IEEE Xplore. They are also included in this report.

Paper Title	Author Names
Image Acquisition And Detection Of The Iris For Iridiology	Petra Perner*, Ibai
Out-Of-Sample Calibration Approach For Classification Methods Based On Spectral Graph Theory	Philippe Belhomme*, Pathimage; Simon Toralba, Pathimage; Benoit Plancoulaine, Pathimage; Myriam Oger, Pathimage-Clcc Baclesse; Catherine Bor, Pathimage-Clcc Baclesse
Detection Of Centroblasts In H&E Stained Images Of Follicular Lymphoma	Emmanouil Michail, ITI-CERTH; Evgenios Kornaropoulos, ITI-CERTH; Kosmas Dimitropoulos, ITI-CERTH; Triantafyllia Koletsa, Aristotle Univ. Of Thessaloniki; Nikos Grammalidis*, ITI-CERTH
Multi-Scale Directional Filtering Based Method For Follicular Lymphoma Grading	Alican Bozkurt*, Bilkent University; Enis Cetin, Bilkent University

Table 1: Technical Program

Day 1			Day 2		
9:00-9-15	Registration				
9:15-9:30	A. E. Cetin-E. Salerno	Welcome Speech			
9:30-10:30	M. Sezgin	Intelligent user interfaces: practical considerations in design and implementation	**9:30-10:30**	Z. Kato	2D and 3D object registration without point correspondences
10:30-10:45	**Coffee Break**		**10:30-10:45**	**Coffee Break**	
10:45-12:45	**Regular Session**		**10:45-12:45**	**Regular Session**	
	B.U Toreyin	Sub-band Decomposition Based Supervised Feature Extraction for Hyperspectral Image Classification		M. Belahcene	Face Recognition Optimization by EFM-PSO
	J. Filip	A Probabilistic Approach to Rough Texture Compression and Rendering		Z. Zdziarski	Extension of GBVS to 3D media
	J. G. Alaydın	Graph-Cut-based Compression Algorithm for Compressed-Sensed Image Acquisition		P. Perner	Our View To Novel Forensic Multimedia Data Analysis
	M. Tofighi	Denoising Using a Framework Based On Projections Onto Convex Sets (POCS)		M. Leszczuk	Key Indicators for Monitoring of Audiovisual Quality
	W. Barhoumi	An Adptive Method for Hierarchical Texture-Based Segmentation		M. Trocan	Content-based Video Fingerprinting Method for Fast Key Generation and Retrieval
12:45-14:00	**Lunch**		**12:45-14:00**	**Lunch**	

14:00-15:00	M.N. Gurcan	Medical Image Analysis: Visual Decomposition and Modeling		**Regular Session**	
15:00-16:45	**MIRACLE Session**		**14:00-15:15**	M. D'Acunto	Radon Transform: Identification of Noise and Instrumental Artifacts
	P. Belhomme	Out-Of-Sample Calibration Approach For Classification Methods Based On Spectral Graph Theory		A. Tonazzini	Non-stationary modeling for the separation of overlapped texts in documents
	A. Bozkurt	Multi-scale directional filtering based method for Follicular Lymphoma grading		D. Khanduja	Segmentation and Recognition Techniques for Handwritten Devanagari Script
	P. Perner	Image Acquisition And Detection Of The Iris For Iridiology	**15:15-15:30**	**Coffee Break**	
	N. Grammalidis	Detection of centroblasts in H&E stained images of follicular lymphoma	**15:30-17:00**	**MUSCLE/MIRACLE Meeting**	
16:45-17:00	**Coffee Break**				
17:00-18:15	**Regular Session**				
	N. Kiryati	Real-Time Embedded System For Road-Crossing Assistance			
	A. Eleyan	Gabor Wavelet Transform Based Facial Expression Recognition Using PCA And LBP			
	I. Cinaroglu	A Direct Approach For Human Detection With Catadioptric Omnidirectional Camera			

Papers Presented in MIRACLE Session

OUT-OF-SAMPLE CALIBRATION APPROACH FOR CLASSIFICATION METHODS BASED ON SPECTRAL GRAPH THEORY

Belhomme Philippe[1], Toralba Simon[1], Plancoulaine Benoît[1], Oger Myriam[2], Bor-Angelier Catherine[1,2]

[1]PATHIMAGE EA 4656, Normandie Université; UNICAEN, CLCC F. Baclesse, Caen, France
[2]Pathology department, CLCC F. Baclesse, Caen, France

ABSTRACT

Spectral graph theory (SGT) relies on the study of properties of a graph in relationship to eigenvalues and eigenvectors of Markov matrices. SGT is commonly used for dimensionality reduction, machine learning (classification, clustering) but is very CPU consuming. This is a problem for "out-of-sample" applications aiming to compare new unknown complex objets to an already built database. In this paper, we present a simple method allowing to get around this problem by adding to Markov matrices some "spy points" later used to calibrate the unknown data with a knowledge database. The spectral graph theory method studied here relies on diffusion maps. Results obtained on artificial images composed of texture samples and on virtual slides of follicular lymphomas are serve to explain the general approach.

Index Terms— Spectral graph theory, manifold learning, virtual slide images, out-of-sample extension

1. INTRODUCTION

Research in signal and image analysis is going on for many decades now and is directly linked with the exceptional development of computer technologies. But after all these years, it must be admit that there are not so many real working applications in practice, especially in the medicine area where the expert's eye is still more accurate and faster than many automated systems dealing with large amounts of data. However, reliable automated systems could really help pathologists in their daily work as the number of pathological cases increases as far as the early screening campaigns do. To illustrate this statement with a medical case, for example images of histological tissue sections, the complex structures to be observed, the very large staining differences encountered with preparations providing from different laboratories and even from the same one, the image file size being more and more large for they are now acquired on digital scanners at higher resolutions (a typical virtual slide image (VSI) is commonly 50 Gb now), all these finally assimilate image processing to the analysis of masses of more or less correlated non-linear data. In some previous works dedicated to the development of a computer-aided diagnosis system (CADS) based on image retrieval and classification [1,2], we have used a method coming from spectral graph theory, the diffusion maps (DM) [3], to process VSI split in small parts called 'patches'. The DM algorithm, in which eigenvalues and eigenvectors of a Markov matrix defining a random walk on the data are computed, allows to both cluster non-linear input data thanks to its inner classification properties preserving local neighborhood relationships, but also to reduce the input data dimensionality in a space (3D concerning this paper) where it is therefore possible to compute euclidean distances between the objects to be analyzed [4,5]. To briefly describe the CADS we are developing, the first step consists in building a knowledge database involving many features extracted from a set of well-known images; this is an 'off-line' procedure conducted once. These features are represented by vectors of non-linear data acting as a signature. In a second step, signatures are obtained from unknown images and then compared with those in the database; this is an 'on-line' procedure that has to be conducted each time a new image is processed.

The diffusion maps technique belongs to unsupervised learning algorithms working only for given training points with no straightforward extension for out-of-sample cases. One of our previous work [6] focused on a way to get around this problem and explained how unknown VSI may be classified by considering the diffusion maps as a learning eigenfunction of a data-dependent kernel. The Nyström formula [7] was thus used to estimate the diffusion coordinates of new data. But even if the Nyström formula approach allowed to drastically limit the computational workload, for the step of eigenvalues and eigenvectors determination has a $O(n^3)$ complexity, the final dimensionality reduction (DimR) result is unfortunately constrained by an intrinsic property of DM. Indeed, with the DM algorithm, the column sum of any eigenvector is always zero and by the way it is directly impossible to compare the projections in a 3D space of two different sets of data points; this is what we will call later the "scaling effect". Moreover, for a given Markov matrix, the absolute values of eigenvector coordinates are independent from the data order (so the order of rows in the matrix) but their sign do. And as the software we are developing mainly deals with parallel computation, the same data set is never processed in the

same order twice; this second effect is later called the "rotation effect".

In this paper, we propose a simple but efficient approach allowing to further decrease the computational workload of the out-of-sample extension of spectral graph theory methods, while making it easier to compare new data sets thanks to the use of "spy points". These "spy points" come from a first set considered as a reference, then are used to fit the other sets in the same 3D space by rotation-scaling of their coordinates. To illustrate our approach in a practical way, we use data sets of feature vectors obtained from image patches extracted in large VSI of follicular lymphomas.

2. MATERIALS

VSI come from histological sections of four different follicular lymphomas stained in the same laboratory according to the Hematoxylin-Eosin-Safron protocol. Images have been acquired by a digital scanner (ScanScope CS; Aperio Technologies) at 20X with a resolution of 0.5 µm per pixel and stored in TIFF 6.0 file format (compression 30%). For this study, histological sections are split in squared areas (also called "patches") of size 100×100 pixels. Each area is then extracted at plain resolution and stored as an uncompressed TIFF image. Tools developed here are written in Python language with the help of specialized modules (PIL: Python Imaging Library, SciPy and mathplotlib).

3. METHODS

3.1. Features extraction

From each patch, statistical parameters based on color and texture information are computed and embedded in a feature vector. They are obtained as global measurements from the RGB color components (reduced to 64 values) and from the two first components (H, E) of the color deconvolution specific to Hematoxylin and Eosin staining [8]. From any given component, the computed features include the mean, median, mode, Skewness and Kurtosis values, the 20%-40%-60%-80% quantiles of its cumulated histogram and 13 Haralick parameters of texture in four directions, that is a total of F=305 features (61×5) per patch. Considering the sparse numerical range of extracted features, the symmetric Kullback-Leibler distance has been retained for its ability to easily manage such values, while remaining fast to implement. The distance between two vectors p_1,p_2 of length F is then given by:

$$D_{KL}\left(p_1, p_2\right)=\frac{1}{2}\sum_{j=1}^{F} p_{1j}.\log\left(\frac{p_{1j}}{p_{2j}}\right)+p_{2j}.\log\left(\frac{p_{2i}}{p_{1j}}\right) \quad (1).$$

3.2. Dimensionality reduction (DimR)

In any classical CADS, one of the key components is a visualization tool showing relationships between supervised images, stored in a knowledge database, and new images that are presented to the system. Typically, these relations may be expressed as a connected graph in a 3D space where one hopes to find distinctive clusters corresponding to histological types or sub-types. It is therefore mandatory to reduce dimensionality from F (F=305 in our application) to just 3. With feature vectors containing non linear data, it is not appropriate to perform a principal component analysis (PCA). In papers [3,4] authors have shown that methods based on Spectral Connectivity Analysis (SCA) such as diffusion maps, involving eigenvalues and eigenvectors of a normalized graph Laplacian, are well suited to non linear data. Let $X=\{x_1,x_2,...,x_n\}$ be a set of n patches that we assimilate to a fully connected graph G, that means a distance function is computed for each pair $\{x_i,x_j\}$. A $n\times n$ kernel P is obtained from a Gaussian function whose coefficients are given by:

$$p\left(x_i,x_j\right)=\frac{w\left(x_i,x_j\right)}{d\left(x_i\right)} \quad (2)$$

with $$d\left(x_i\right)=\sum_{x_k\in X} w\left(x_i,x_k\right) \quad (3)$$

and $$w\left(x_i,x_j\right)=e^{-\left\{\frac{D_{KL}\left(x_i,x_j\right)}{\epsilon}\right\}} \quad (4).$$

In fact, $p(x_i,x_j)$ may be considered as the transition kernel of the Markov chain on G. In other words, $p(x_i,x_j)$ defines the transition probability for going from x_i to x_j in one time step. The eigenvectors φ_k of P, ordered by decreasing positive eigenvalues, give the practical observation space axes. It must be noticed that φ_0 is never used since linked to the eigenvalue λ=1 (i.e. the data set mean or trivial solution). The 3D projection is then achieved along (φ_1,φ_2,φ_3). Choosing ε in $w(x_i,x_j)$ is an empirical task which should permit a moderate decrease of the exponential in equation (4); some works [4] use the median value of all $D_{KL}(x_i,x_j)$ distances whereas other works [5] use the mean distance obtained in the k nearest neighbors from a subset of X. We have retained the first solution.

3.3. Out-of-sample extension

3.3.1. Nyström formula

SCA techniques share one major characteristic that is to compute the spectrum of a positive definite kernel. It is known that the eigenvalue decomposition of a matrix $P \in \mathbb{R}^{n\times n}$ can be computed no faster than $O(n^3)$; this limits SCA techniques to moderately sized problems [9]. Fortunately the Nyström extension, originally applied for finding numerical solutions of integral equations, can be used to compute eigenvectors and eigenvalues of a sub-matrix formed by m columns of P randomly subsampled and then extended to the remaining n-m columns [7]. Given an $n\times n$ matrix P and an integer $m<n$. Let call $P^{(m)}$ the matrix formed by m columns of P that is the graph Laplacian of a set $Y\subset X$ with $|Y|=m$. Y is then a training set. The orthonormal matrix of eigenvectors $U^{(m)}$ and their associated eigenvalues in a diagonal matrix $\Lambda^{(m)}$ are classically obtained from $P^{(m)}$ by solving: $P^{(m)}U^{(m)}=\Lambda^{(m)}U^{(m)}$. This step has to be run once and then may be considered as an 'off-line' procedure. The Nyström formula allows to obtain the approximate eigenvectors of all the set X by:

$$\hat{u}_i = \sqrt{\frac{m}{n}}\frac{1}{\lambda_i^{(m)}} P_{N,M}\, u_i^{(m)} \qquad (5)$$

where $\lambda_i^{(m)}$ and $u_i^{(m)}$ are the i^{th} diagonal entry and i^{th} column of $\Lambda^{(m)}$ and $U^{(m)}$ respectively. $P_{N,M}$ is a $n\times m$ sub-matrix of the complete graph obtained from distances $w(x_i,x_j)$. Its computation is an 'on-line' procedure having to be conducted for each new test set ($X\backslash Y$). For a 3D visualization, the second to fourth columns are used (the first one being the trivial solution).

3.3.2. "Linear Spy Points" (LSP) approach

The DimR procedure achieved thanks to the diffusion maps yields to a set of data points where the column sum of each eigenvector is necessarily equal to 0. Therefore, each new test run provides a set of coordinates that cannot be compared to a previous computation. The approach explored in this "linear spy points" section consists in simply run each test with a set of 3 data points further used as a reference. In the original 3D space $\mathscr{E}$, 3 spy points corresponding to 3 patch images are selected and expressed by A(X_A,Y_A,Z_A), B(X_B,Y_B,Z_B) and C(X_C,Y_C,Z_C). Then, for each new test run, these 3 patches are first added in the directory where the other 'unknown' patches stand and the DimR procedure is processed. The 3 spy points become A',B',C' and are now expressed by A'(x_A,y_A,z_A), B'(x_B,y_B,z_B) and C'(x_C,y_C,z_C) in the new space $\mathscr{E}'$. If we assess that going from A',B',C' to A,B,C is just a linear transform, thus any point *in* $\mathscr{E}'$ will be expressed from its corresponding element in $\mathscr{E}'$ by a linear vectorial expression as in equation (6).

By using A,B,C and A',B',C' coordinates in (6), the nine matrix elements are easily found by resolving the nine independent linear equations, thus providing the transformation matrix M between $\mathscr{E}'$ and $\mathscr{E}$.

$$\begin{pmatrix} X \\ Y \\ Z \end{pmatrix} = \begin{bmatrix} a_x & b_x & c_x \\ a_y & b_y & c_y \\ a_z & b_z & c_z \end{bmatrix} \cdot \begin{pmatrix} x \\ y \\ z \end{pmatrix} \qquad (6)$$

4. RESULTS AND DISCUSSION

4.1. Nyström formula

As the DM method preserves the local proximity between data points, DM+Nyström thus allow to compare a new data set of size n-m with a knowledge database of size m. Fundamentally, this is not a real calibration process since the n total points are embedded in a 3D space which is different from both the space where the m points and the n-m points were obtained. Moreover, the space properties depend on m. Fig. 1 shows the Nyström extension for n-m=1000 patches applied on m=1000 references, compared with the raw computation on the 2000 patches (patches come from breast cancer images from the study cited in [6]). Fig. 2 shows the same approach with n-m=1500 points and m=500. In the second case, it may be noticed that the red point cloud keeps quite the same shape than the black point cloud but is located much more far away from it than with m=1000.

4.2. "Linear Spy Points" approach

In order to test if a linear transformation matrix may be used with DM, an artificial image I composed of texture samples coming from the Brodatz database [XX] has been created. At the beginning, I is processed as a whole and 3 spy points are randomly selected under a constraint on a minimal euclidean distance between them in the 3D reference space $\mathscr{E}_{ref}$. I is then split in 2 equal parts (I_1 and I_2) which are processed independently but with the set of spies, so projected in 2 different 3D spaces $\mathscr{E}'$ and $\mathscr{E}$. Once the linear transformation matrices are computed and applied on all data points, $\mathscr{E}'$ and $\mathscr{E}$ are supposed to match $\mathscr{E}_{ref}$. To better represent this approach, spaces $\mathscr{E}$, $\mathscr{E}'$ and $\mathscr{E}_{ref}$ with their own orthonormal coordinate system (φ_1,φ_2,φ_3) are assimilated to RGB color cubes in which each point is associated with a false color. A reliable calibration process would be encountered if the two half colormaps obtain on I_1,I_2 really match the colormap of I.

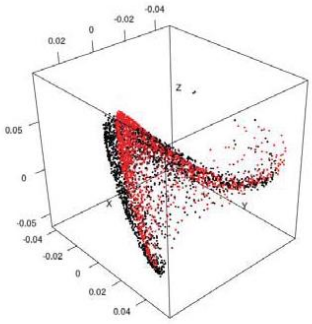

Figure 1: 2000 true eigenvectors coordinates (black dots) vs estimated coordinates obtained from 1000 points (red dots).

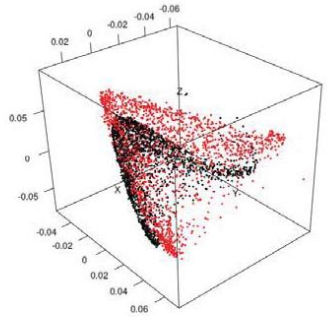

Figure 2: 2000 true eigenvectors coordinates (black dots) vs estimated coordinates obtained from 500 points (red dots).

Figure 3 shows the main steps of the *LSP* approach. Starting from the original image I (top-middle), I is split in 2 parts (arrows 1) I_1 and I_2. I is processed as a whole to obtain its colormap C_{ref} in $\mathscr{E}_{ref}$ (arrow 2). I_1 and I_2 are independently processed (arrows 4) and their corresponding colormaps C_1 and C_2 are respectively obtained in $\mathscr{E}_1$ and $\mathscr{E}_2$. The *LSP* approach is applied to match $\mathscr{E}_1$ with $\mathscr{E}_{ref}$ and $\mathscr{E}_2$ with $\mathscr{E}_{ref}$ (arrows 5). The 2 colormaps are combined (arrows 6) and C_{1+2} is compared to the C_1 (arrows 7). With an artificial image such as the one we used here, the LSP approach yields to a final colormap C_{1+2} that is visually close to the reference C_{ref}. The mean value of all color differences between C_{1+2} and C_{ref} is about 6%, with a maximal value of 21%.

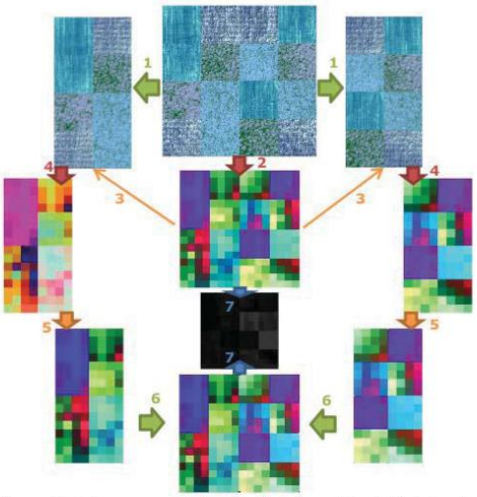

Figure 3: Linear spy point procedure to calibrate 2 data sets successively computed in a dimensionality reduction scheme by the diffusion maps.

Not finished yet for follicular lymphomas (FL)... The paper length needs also to be reduced to add results and images for FL.

5. CONCLUSION

The linear spy point approach exposed in this paper is a first answer to the problem of out-of-sample extension encountered with dimensionality reduction methods such as the diffusion maps. Unfortunately, for non-linear input data, it cannot be a real solution. The next way that will be explored is to work on a non-linear spy point approach taking into account much more spy points whose coordinates come from the Nyström formula.

6. REFERENCES

[1] M. Oger, P. Belhomme, J. Klossa, J.J. Michels and A. Elmoataz, "Automated region of interest retrieval and classification using spectral analysis", *Diagnostic Pathology*, 3(Suppl 1):S17, 2008.

[2] P. Belhomme, M. Oger, J.J. Michels, B. Plancoulaine and P. Herlin, "Towards a computer aided diagnosis system dedicated to virtual microscopy based on stereology sampling and diffusion maps", *Diagnostic Pathology*, 6(Suppl 1): S3, 2011.

[3] R.R. Coifman, S. Lafon, A.B. Lee, M. Maggioni, B. Nadler, F. Warner and S. Zucker, "Geometric diffusions as a tool for harmonics analysis and structure definition of data: Diffusion maps", *Proceedings of the National Academy of Sciences*, 102(21), pp. 7426-7431,2005.

[4] M. Belkin and P. Niyogi, "Laplacian eigenmaps for dimensionality reduction and data representation", *Neural Computation*, vol. 15, pp. 1373-1396, 2003.

[5] R.R. Coifman, S. Lafon, "Diffusion maps", *Applied and Computational Harmonic Analysis*, vol. 21, Issue 1, pp. 5-30, 2006.

[6] P. Belhomme, M. Oger, J.J. Michels and B. Plancoulaine, "Out-of-sample extension of diffusion maps in a computer aided diagnosis system. Application to breast cancer virtual slide images", *Diagnostic Pathology*, 8(Suppl 1): S9, 2013.

[7] C. Williams and M. Seeger, "Using the Nyström method to speed up kernel machines", *Advances in Neural Information Processing Systems*, vol. 13, pp. 682-688, 2011.

[8] A.C. Ruifrok and D.A. Johnston, "Quantification of histochemical staining by color deconvolution", *Anal Quant Cytol Histol*, vol. 23, pp. 291-299, 2001.

[9] D. Homrighausen and D.J. McDonald, "Spectral approximations in machine learning", *ArXiv*:1107.4340, July 2011.

MULTI-SCALE DIRECTIONAL FILTERING BASED METHOD FOR FOLLICULAR LYMPHOMA GRADING

Alican Bozkurt, A. Enis Cetin

Bilkent University
Department of Electrical and Eletronics Engineering
TR-06800, Bilkent, Ankara, Turkey

ABSTRACT

Follicular Lymphoma(FL) is a group of malignancies of lymphocyte origin that arise from lymph nodes, spleen, and bone marrow in the lymphatic system in most cases and is the second most common non-Hodgkins lymphoma. Characteristic of FL is the presence of follicle center B cells consisting of centrocytes and centroblasts. One common way of grade FL images is an expert manually counting the centroblasts in an image, which is time consuming. In this paper we present a novel multi-scale directional filtering scheme, and utilize it to classify FL images into differnet grades. Instead of counting the centroblasts individually, we classify the texture formed by centroblasts. We apply our multiscale-directional filtering scheme in 2 scales and along 8 orientations; and use mean and standard deviation of each filter output as features. For classification, we use support vector machines with radial basis function kernel. We map the features into two dimensions using linear discriminant analysis prior to classification. When SVM parameters are optimized, this method achieves $100,0\%$ 10-fold cross validation accuracy on a 270-image dataset.

Index Terms— One, two, three, four, five

1. INTRODUCTION

Follicular Lymphoma(FL) is a group of malignancies of lymphocyte origin that arise from lymph nodes, spleen, and bone marrow in the lymphatic system in most cases and is the second most common non-Hodgkins lymphoma [1]. Characteristic of FL is the presence of a follicular or nodular pattern of growth presented by follicle center B cells consisting of centrocytes and centroblasts. World Health Organization's (WHO) histological grading process of FL depends on the number of centroblasts counted within representative follicles, resulting in three grades with increasing severity [2]:

Grade 1 0-5 centroblasts(CBs) per high-power field (HPF)

Grade 2 6-15 centroblasts per HPF

Grade 3 More than 15 centroblasts per HPF

Therefore, accurate grading of follicular lymphoma images is of course essential to the optimal choice of treatment. One common way of grade FL images is an expert manually counting the centroblasts in an image, which is time consuming. Recently. Suhre proposed 2-level classification tree using sparsity-smoothed Bayesian classifier, and reported very high accuracies [3].

The dataset provided by [3] is also used in this paper. The dataset consists of 90 images for each of 3 grades of Follicular Lymphoma. In Follicular Lymphoma Grading problem, we aim to grade microscope images according to their centroblast counts. Instead of counting the centroblasts individually, we try to classify the texture formed by centroblasts.

2. DIRECTIONAL FILTERING FRAMEWORK

Directional filtering is a new framework developed in this paper. In this framework, we start with a given filter impulse response f_0 with filter length N in one-dimension (1D) and we wish to use f_0 to filter images in various directions. To do so, we propose to create a set of filters obtained by rotating f_0 along a set of angles parameterized by θ.

Instead of rotating f_0 by bilinear (or cubic) interpolation, we use the following method: For a specific angle θ, we draw a line l going through origin ($l : y = \tan\theta x$) and determine the coefficients of the rotated filter $f_\theta(i,j)$ proportional to the length of the line segment within each pixel (i,j), which is denoted by $|l_{i,j}|$. For odd N, $f_0(0)$ is exactly the center of rotation, therefore value of $f_0(0)$ does not change in $f_\theta(0,0)$. Therefore we take line segment in origin pixel $|l_{0,0}|$ as reference ($|FG|$ in Figure 1(b)). For $\theta \leq 45°$, $|l_{0,0}| = \frac{1}{\cos\theta}$, assuming each pixel is of unit side. For each pixel in column j in the grid, we calculate the $f_\theta(i,j)$ as $f_\theta(i,j) = f_0(i) \times \frac{|l_{i,j}|}{|l_{0,0}|}$. This approach is also used in computerized tomography [4].

Calculating the line segment $|l_{i,j}|$ is straightforward. To rotate the filter for $\theta \leq 45°$ (which corresponds to $N_v \leq 1$), we place f_0 to the vertical center of a $N \times N$ grid, where $C_X(i,j)$ and $C_Y(i,j)$ are the coordinates of the center of cell with horizontal index $i = 0,\ldots,N-1$, and vertical index $j = 0,\ldots,N-1$. Then we construct a line l along the de-

sired direction where the bisector of the line is the exact center of the grid (which is also the center of filter). For every cell of the grid, we calculate the rotated filter coefficients as : $f_\theta(i,j) = f_0(i,j) \times \max(0, 1 - C_(i,j) + l(C_x(i,j)))$. To rotate the filter for $\theta \geq 45°$ we first rotate the filter $90° - \theta$ then transpose $f_{90°-\theta}$ to get f_θ. Note that this method of rotation retains the DC response of the original filter, since $\sum_{i,j} f_\theta(i,j) = \sum_k f_0(k)$.

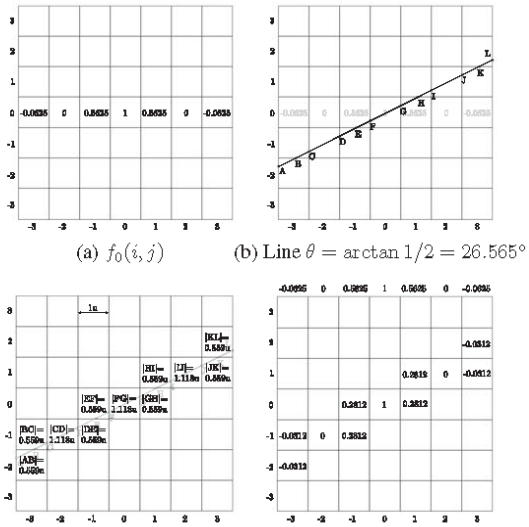

(a) $f_0(i,j)$ (b) Line $\theta = \arctan 1/2 = 26.565°$

(c) Lengths of line segments in each pixel (d) Resulting $f_{26.56°}$

Fig. 1. Filter rotation process for Lagrange *à trous* filter

This method imposes a lower bound on θ, since at the line should cross at least one pixel other than original pixels of f_0. Assuming $C_x(i,j) = i$ and pixels have side l, this bound is calculated as follows:

$$\tan(\theta)[C_x(\frac{N-1}{2}, 0) + l/2] \geq \frac{l}{2} \quad (1)$$

$$\tan(\theta) \geq \frac{1}{2C_x(\frac{N-1}{2}, 0) + 1} \quad (2)$$

$$\tan(\theta) \geq \frac{1}{N} \quad (3)$$

$$\theta \geq \arctan(\frac{1}{N}) \quad (4)$$

Resulting filters form a directional filter bank are shown in the first row of Table 1. These directional filters are used in a multi-resolution framework for feature extraction. For the first scale, directional images can be extracted by convolving the input image with this filter bank. Mean and standard of these directional images are used as the directional feature values of the image (other statistics, or the image itself can also be used). To obtain direction feature values at lower scales, the original image is low-pass filtered and decimated by a factor of two horizontally and vertically and a low-low sub-image is obtained. Since downsampling is a shift variant process, we also introduce a half-sample delay before downsampling. To implement this, we downsample two shifted versions of input image (corresponding to $(\Delta x, \Delta y) = \{(0,0),(1,1)\}$), pass two downsampled images from our directional filter bank, and fuse the outputs to construct one output image per filter in directional filter bank. Fusing method used in thesis is simply taking square of images, summing them, and taking the square root of the sum.

Table 1. Directional and rotated filters for $\theta = \{0°, \pm 26.56°, \pm 45°, \pm 63.43°, 90°\}$

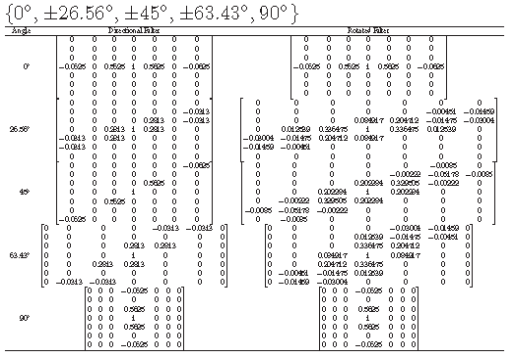

A variant of this multi-scale filtering framework uses four shifted versions instead of two (corresponding to $(\Delta x, \Delta y) = \{(0,0),(1,0),(0,1),(1,1)\}$). Although this increases the accuracy by average 1%, it also doubles the computational complexity. This speed vs. accuracy trade-off should be evaluated for potential applications.

The lowpass filter used in downsampling f_0 can be the corresponding lowpass filter of a wavelet filter bank. If f_0 is chosen as such, or it can be a simple half-band filter. The low-low sub-image can be filtered by directional filters to obtain the second level directional subimages and corresponding feature values. This process can be repeated several times depending on the nature of input images. The filtering flow diagram is shown in Figure 3.

In our experiments we use directional filters in 3 scales, $\theta = \{0°, \pm 26.56°, \pm 45°, \pm 63.43°, 90°\}$ and lowpass filter is halfband filter $f_l = [0.25\ 0.5\ 0.25]$. For filter bank we use Kingsburys $8th$ order q-shift analysis filter [5]: $f_0 = [-0.0808\ 0\ 0.4155\ -0.5376\ 0.1653\ 0.0624\ 0\ -0.0248]$

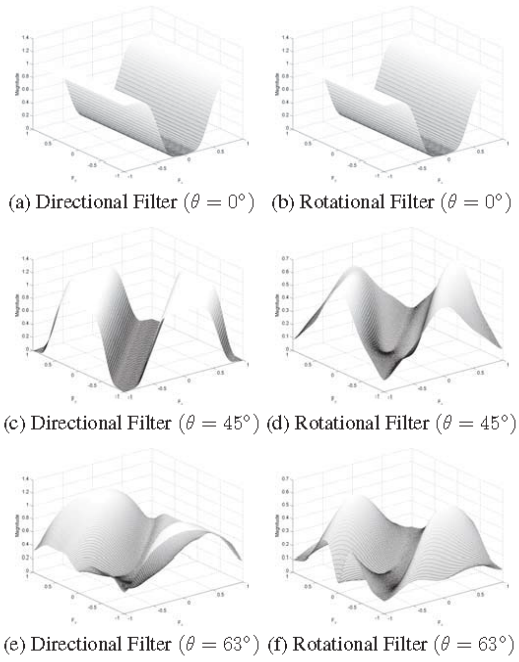

(a) Directional Filter ($\theta = 0°$) (b) Rotational Filter ($\theta = 0°$)

(c) Directional Filter ($\theta = 45°$) (d) Rotational Filter ($\theta = 45°$)

(e) Directional Filter ($\theta = 63°$) (f) Rotational Filter ($\theta = 63°$)

Fig. 2. Frequency Responses of directional and rotated filters at various orientations.

3. FEATURE EXTRACTION AND CLASSIFICATION

Since images in this dataset are of relatively uniform texture, there is no need to segment the images prior to feature extraction. Also, It is not possible to have 2 different grades of lymphoma in an image, so we give one decision per image. We take take input image and feed it to feature extraction algorithms directly after converting to grayscale. After feature extraction, we experiment with dimension reduction. Each feature is classified once without any dimension reduction, once after principal component analysis (PCA) [6], and once after linear discriminant analysis (LDA) [7]. For PCA, dimension is reduced keeping the 99.9% of the cumulative energies of eigenvalues. For LDA, since the maximum number of dimensions is bounded by the number of classes, dimension is reduced to 2D for each feature.

By definition, all multi-dimensional directional feature extraction algorithms output features as a filter response for each scale-direction pair. These filter outputs cannot be used directly as features because they are variant to size of input window, scale, small perturbations in input image such as translation or rotation. In order to make the feature more standardized and more robust to these factors, we

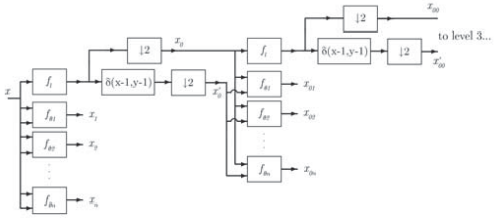

Fig. 3. Image flowchart directional filtering framework

use mean and standard deviation of filter outputs for each scale-direction pair. If we use filter outputs of a 3-scale and 6-directional feature extraction algorithm directly, we cannot say anything about the size of our feature vector: it depends on the size of input image. Also, even if we assume the input is just 24×24 pixels, the feature size would be $6 \times 24 \times 24 + 6 \times 12 \times 12 + 6 \times 6 \times 6 = 42552$, which is too large to classify efficiently. If we use mean and standard deviation of filter outputs for the same algorithm, we easily see that the feature size is $2 \times 3 \times 6 = 36$ regardless of the input. Then we classify the extracted features using Support Vector Machines (SVM) with Radial Basis Function (RBF) as kernel function. The accuracy of the system, as mentioned before, is measured by 10-fold cross validation, which is a very standard method for measuring the accuracy of classification in the literature. In order to find optimal accuracy, we perform a parameter search for C and γ parameters of SVM using simple heuristics.

4. RESULTS

We compare the proposed features with various multi-scale directional feature extraction algorithms, such as curvelets [8], contourlets [9], steerable pyramids [10], complex wavelets [11], Gabor filters [12], texton filterbanks [13, 14, 15],and Gray-level co-occurrence matrices [16]. We also compare our results with state of the art [3].

Furthermore, we also performed tests to measure the computational complexity of algorithms. These tests are done on a computer with Intel i7-4700MQ CPU and 16 GB memory. Values presented in Table 3 are average times over 10 runs. It is clear that directional filters are the most efficient among tested algorithms.

5. CONCLUSION

A method for grading follicular lymphoma images, based on a novel multi-scale directional feature extraction framework is proposed. In this framework we draw a line l going through origin ($l : y = \tan\theta x$) for a specific angle θ, and determine the coefficients of the rotated filter $f_\theta(i, j)$ proportional to

Table 2. 10-fold cross-validation accuracies of each grade, for each feature

Feature	Dimension Reduction	Grades			Mean
		Grade 1	Grade 2	Grade 3	
CWT	LDA	100.00	98.88	100.00	99.63
	PCA	76.67	76.40	70.00	74.36
	None	96.67	98.88	98.89	98.14
LM	LDA	98.89	100.00	100.00	99.63
	PCA	80.00	92.13	90.00	87.38
	None	95.56	93.26	100.00	96.27
MR8	LDA	95.56	94.38	100.00	96.65
	PCA	65.56	73.03	90.00	76.20
	None	97.78	92.13	98.89	96.27
Contourlet	LDA	100.00	8.99	100.00	69.66
	PCA	82.22	82.02	84.44	82.90
	None	87.78	88.76	100.00	92.18
Curvelet	LDA	95.56	4.49	100.00	66.68
	PCA	78.89	93.26	98.89	90.35
	None	84.44	96.63	98.89	93.32
Dir. Fil	LDA	100.00	100.00	100.00	100.00
	PCA	71.11	80.90	85.56	79.19
	None	97.78	97.75	98.89	98.14
Gabor	LDA	0.00	0.00	100.00	33.33
	PCA	83.33	86.52	90.00	86.62
	None	86.67	89.89	95.56	90.70
GLCM	LDA	88.89	88.76	86.67	88.11
	PCA	22.22	34.83	47.78	34.94
	None	85.56	86.52	85.56	85.88
Pyramid	LDA	98.89	98.88	100.00	99.26
	PCA	71.11	94.38	67.78	77.76
	None	96.67	94.38	98.89	96.65
[3]	None	98.89	98.89	100.00	99.26

the length of the line segment within each pixel (i, j). This new multi-scale directional framework is compared with a number of multi-scale directional image representation methods including the complex wavelet transforms, curvelets, contourlets, gray level co-occurrence matrices, Gabor filters, steerable pyramids, and texton filter banks.

In terms of computational efficiency, directional filter banks are the fastest among all tested methods, extracting features from a 512×512 image in 8 directions and three scales in 0.032 seconds.

When features extracted with proposed method are reduced to 2D using linear discriminant analysis, a SVM classifier with optimum parameters achieves 100% 10-fold cross-validation accuracy, surpassing other multi-scale directional feature extraction algorithms and state of art.

Table 3. Time required for each feature to be extracted from a $N \times N$ image, for $N = [512, 1024, 2048]$

Feature	Required time per $N \times N$ sample (s)		
	N=512	N=1024	N=2048
CWT	0.0615	0.277	1.2129
Curvelet	0.1863	0.7188	3.3451
Contourlet	0.178	0.6051	2.5417
GLCM	0.3643	1.6249	6.6618
Gabor	0.9655	3.9268	16.1438
Pyramid	0.2714	1.4155	6.1437
Dir. Fil.	0.0323	0.1343	0.5447
MR8	0.2083	0.8757	3.4984
LM	2.1083	7.2679	32.69
RFS	1.6273	5.8382	25.7325

6. REFERENCES

[1] M Garcia, AWECMHYSRTMJ Jemal, EM Ward, MM Center, Y Hao, RL Siegel, and MJ Thun, "Global cancer facts & figures 2007," *Atlanta, GA: American Cancer Society*, vol. 1, no. 3, 2007.

[2] Elaine S Jaffe, "The 2008 who classification of lymphomas: implications for clinical practice and translational research," *ASH Education Program Book*, vol. 2009, no. 1, pp. 523–531, 2009.

[3] Alexander Suhre, *Novel Methods for Microscopic Image Processing, Analysis, Classification and Compression*, Ph.D. thesis, Bilkent University, 2013.

[4] Gabor T Herman and Attila Kuba, *Discrete tomography: Foundations, algorithms, and applications*, Springer, 1999.

[5] N. Kingsbury, "A dual-tree complex wavelet transform with improved orthogonality and symmetry properties," in *Image Processing, 2000. Proceedings. 2000 International Conference on*. IEEE, 2000, vol. 2, pp. 375–378.

[6] Ian Jolliffe, *Principal component analysis*, Wiley Online Library, 2005.

[7] C Radhakrishna Rao, "The utilization of multiple measurements in problems of biological classification," *Journal of the Royal Statistical Society. Series B (Methodological)*, vol. 10, no. 2, pp. 159–203, 1948.

[8] Emmanuel Candes, Laurent Demanet, David Donoho, and Lexing Ying, "Fast discrete curvelet transforms," *Multiscale Modeling & Simulation*, vol. 5, no. 3, pp. 861–899, 2006.

[9] Minh N Do and Martin Vetterli, "The contourlet transform: an efficient directional multiresolution image representation," *Image Processing, IEEE Transactions on*, vol. 14, no. 12, pp. 2091–2106, 2005.

[10] Eero P Simoncelli and William T Freeman, "The steerable pyramid: A flexible architecture for multi-scale derivative computation," in *Image Processing, 1995. Proceedings., International Conference on*. IEEE, 1995, vol. 3, pp. 444–447.

[11] Nick Kingsbury, "Image processing with complex wavelets," *Phil. Trans. Royal Society London A*, vol. 357, pp. 2543–2560, 1997.

[12] N. Petkov and M.B. Wieling, "Gabor filter for image processing and computer vision," Tech. Rep., University of Groningen, 2008.

[13] Jitendra Malik, Serge Belongie, Jianbo Shi, and Thomas Leung, "Textons, contours and regions: Cue integration in image segmentation," in *Computer Vision, 1999. The Proceedings of the Seventh IEEE International Conference on*. IEEE, 1999, vol. 2, pp. 918–925.

[14] Thomas Leung and Jitendra Malik, "Representing and recognizing the visual appearance of materials using three-dimensional textons," *International Journal of Computer Vision*, vol. 43, no. 1, pp. 29–44, 2001.

[15] Cordelia Schmid, "Constructing models for content-based image retrieval," in *Computer Vision and Pattern Recognition, 2001. CVPR 2001. Proceedings of the 2001 IEEE Computer Society Conference on*. IEEE, 2001, vol. 2, pp. II–39.

[16] Robert M Haralick, Karthikeyan Shanmugam, and Its' Hak Dinstein, "Textural features for image classification," *Systems, Man and Cybernetics, IEEE Transactions on*, , no. 6, pp. 610–621, 1973.

IMAGE ACQUISITION AND DETECTION OF THE IRIS FOR IRIDIOLOGY

Petra Perner

Institute of Computer Vision and applied Computer Sciences, IBaI
Kohlenstr. 2, 04107 Leipzig, Germany
pperner@ibai-institut.de, www.ibai-institut.de

ABSTRACT

The iris of a human is not only relevant for biometry; it is also relevant for the prediction and diagnosis of human health. One understands by iris diagnosis (Iridology) the investigation and analysis of the colored part of the eye, the iris, to discover factors which play an important role for the prevention and treatment of illnesses. Up-to-date the iris diagnosis is done manually and is concerned with the know problems, objectivities and reproducibility. An automatic system would pave the way for much wider use of the iris diagnosis for the diagnosis of ill-nesses and for the purpose of individual health protection. In this paper we describe the state-of-the-art of the Iridology. Different ways of image acquisition and image preprocessing are explained. We describe the image analysis method for the detection of the iris. This method is based on our novel case-based object recognition and case mining method.

Index Terms— Iris diagnosis, biometry, recognition method, image acquisition

1. INTRODUCTION

The iris of a human is not only relevant for biometry; it is also relevant for the predic-tion and diagnosis of the health of a human. The later is called iris diagnosis.

One understands by iris diagnosis (Iridology) [1] the investigation and analysis of the colored part of the eye, the iris, to discover factors which play an important role for the prevention and treatment of illnesses, but also for the preservation of an optimum health [2-4].

One of the advantages of the iris diagnosis consists in the fact that it is able to provide a lot about the state of the health of a person. An iris picture can point out a health problem. For example, the fact that more than only one single organ is concerned or that the problem also has an emotional or mental component. Thus one can discuss much better with a patient who must decide between different possibilities of treatment much better or initiate preventive measures before the illness comes to the outbreak.

The iris diagnosis has set up in many countries a complementary-medicine discipline [5-8] . Thanks to her special qualities the iris diagnosis is able to cross some borders which have been established in the last decades with the heavyweight on „evidence-based medicine“ in the medical science. The iris diagnosis is an easy diagnostic method that gets by without big apparatus expenditure and the costs linked with it. It gives to general doctors and also other holistically working therapists a secured diagnosis instrument in the hand.

The iris diagnostic is one of few disciplines which pull up the eye for the diagnosis position. Ophthalmologists already know this; they judge the ocular inside around illnesses to ascertain. Besides, they know some illness signs with which the iris diag-nosis works and they are of use already.

In addition, there are investigations with the help of the irises to derive the constitutional type namely the basic disposition of the individual as well as his personality picture. This constitution decides on it for which problems and illnesses an individual is especially susceptible. Moreover, the preserved information about the personality type can be pulled up for the composition of teams.

The aim of the project is to develop an automatic iris image acquisition and diagnosis system. The development of algorithms and procedures for the analysis of the structure inside the iris, the color information and the patterns on the irises that can be automatically used together with the expert's knowledge on illness pictures.

The image acquisition and the preprocessing is describe in Section 2. The case-based object recognition method is described in Section 3. Results on the image acquisition, the preprocessing, and the recognition of the iris are given in Section 4. Finally, we give conclusions in Section 5.

2. IMAGE ACQUISITION

The aim of this work was to develop an easy useable image acquisition unit that allows a person to inspect his iris by himself.

To understand the conditions necessary for iris image acquisition, we first started with the normal microscopic setting of the ophthalmologist. This image acquisition unit consists of an ophthalmologist microscope with a special locking of the head, a white lamp and a digital camera

CANON AS 710. The magnification of the lens is 450 xs. The light is irradiated into the eye with an angle of 45grad. Note, the eye ball is a moving objects therefore it is not possible to position the light reflex point into a certain part object of the eye.

The image has been taken by a human after having found the right focus level and a sharp image. The resulting digital images are shown in Figure 1a-b.

It is a single shot image not a movie. Such an image acquisition unit cannot be used by human by himself.

Fig. 1a The image cut out of the microscope

Fig. 1b The rectangular cut out of the image in Fig. 1a

The second choice was a handheld microscope with a ring of four white light lamps and a 400x magnification. The microscope was equipped with a gum eye mus-cle infront of the microscope to ensure safety image acquisition for the person, no foreign light irradiation and a defined image acquisition distance to the object. There is still a manual focus. A sequence of images is taken and the best images of this sequence are cut out for further evaluation. Some sample images of three different subjects are shown in Fig. 2a-c.

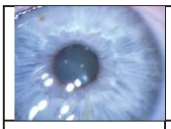

Fig. 2a Iris of Subject1

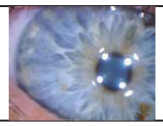

Fig. 2b Iris of Subject2

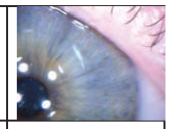

Fig. 2c Iris of Subject3

The iris is never fully centered in the image. Sometimes we get only part of the iris. Sometimes we have the lid in the image and sometimes not. That is because we cannot lock the eye in front of the camera. The light reflection points are a bit annoyingly. However, that are white spots in the image and they can easily be removed. Unfortunately the area under the white spots is not useable for diagnosis anymore. The setting of the light reflection points into the pupil would be much more preferable but since the eye is moving it is almost impossible unless the observer is waiting for the time were the light reflection points are perfectly located inside the pupil.

3. DETECTION OF THE IRIS BY CASE-BASED OBJECT RECOGNITION

We first need to find a reference point in the image. Our reference point is the pupil of the eye. From the center of the pupil we set out a circular model and match this model against the image contours. Where the image points give the best fit with the model is the boundary of the iris located. Based on the color we can judge how much area the iris will cover in the image. The iris is colored while the surrounding is white or skin-type color.

The model can be a general model such as a circle or different types of models taken from different example images such as described in [10]. We choose the later approach and use case-based object recognition [9] [11] for the detection of the iris.

3.1. CASE-BASED OBJECT RECOGNITION

The heart of our case-based object recognition system is a case base of shapes. These shapes are represented as contour chains. Therefore a case is comprised of a set of contour Points $S_c = \{s_c(x_o, y_o); 1 \le c \le n\}$ where each contour point has the grey value 1 and a class label for the shape. Based on this information we can transform the shape from the contour point list into a 2-D image matrix, further called case image. The case base is filled up for the actual application by shapes that we learnt based on our novel case acquisition and case mining method [10]. An index over the case base should allow us to find the closest case among the numerous cases in short time. A case image is matched against the image by constructing an image pyramid from the actual image and the case image. This allows us to reduce the computation time while matching.

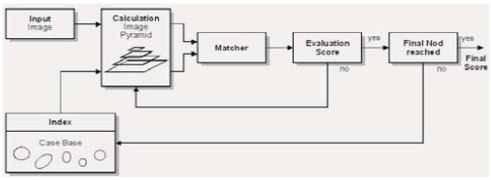

Figure 3. Architecture of a Case-Based Object Recognition System

Beginning with the highest level of the image pyramid the scores are calculated and the areas of interest are marked. The area of interest is the area where an object can be detected. This area is recursively used for further matching by going downward the levels of the image pyramid. Finally the closest match is given to the output. Depending on the actual value of the similarity measure the next level of the

index structure is selected and the process repeats until a final node is reached. The architecture of our case-based object recognition system is shown in Figure 3.

3.2. Case Representation

In general, we can distinguish between three different case representations according to the pixels that are used for matching:

1. Region of Interest (ROI): A region of interest ROI is obtained by taking a cut-out from the original image. All pixels of the obtained image matrix are used as case pixels regardless if they are object or background pixels.
2. Object Case: In the image matrix shown in Figure 2b are only used those pixels as case points that lie inside and at the contour of the object. In this case the shape and the inner structure of the object are taken into consideration.
3. Contour Case: Only pixels that lie on the contour of an object are taken as case points. Thus only the shape of the object of interest is matched.

The kind of representation used for the cases depends on the special image quality the matcher should detect. Our goal is to recognize the fungi spores. To use an object case would not be sufficient for our application since the appearance of the structure inside the objects is very diverse and because of that it would result in a case base where for each case is stored an object. The only representation that gives us a more generalized view to the objects is the shape. Therefore we use a contour case as case representation.

Note that an object might appear in an image with different size and under a different rotation angle and on various locations in an image. But it is still the same object. It makes no sense to store all these identical but different sized and rotated objects in the case base. Rather there should be stored a unit object with the origin coordinates *x0* and *y0* that can be translated, resized and rotated during the matching process. Therefore the case pixels $p_k = (t_k, u_k)^T$ and the direction vectors $m_k = (v, w)^T$ have to be transformed with a matrix A to:

$$\begin{aligned} p'_k &= A \cdot p_k \\ m'_k &= A \cdot m_k \end{aligned} \qquad (1)$$

If φ denotes the angle of rotation and r the scaling factor the matrix may look like the following:

$$A = \begin{pmatrix} a_{11} & a_{12} \\ a_{21} & a_{22} \end{pmatrix} = \begin{pmatrix} r\cos\varphi & -r\sin\varphi \\ r\sin\varphi & r\cos\varphi \end{pmatrix} \qquad (2)$$

Subheadings should appear in lower case (initial word capitalized) in boldface. They should start at the left margin on a separate line.

3.3. Image Representation

Since we are looking for the contour of the object which is the boundary between the background and the object and which is usually an area of high grey level chance we are representing the image by the edges. The edges can be represented by the gradient of the pixels. In order to determine the gradient, first the direction vector of a pixel at the position is calculated from the grey level matrix. The direction vector indicates the change of the grey value in vertical and horizontal direction respectively. The length of this vector is equal to the gradient and it is commonly determined from the direction vector through the following formula:

$$\left\| \vec{z}_{(x,y)} \right\| = \sqrt{(\Delta x)^2 + (\Delta y)^2} \qquad (3)$$

Due to the discreteness of the grey level matrix which represents the grey value function only in some well-chosen points, the direction vectors cannot be calculated by the known analytic derivation formula. Therefore many operators were developed that allow us to determine the direction vectors from the grey level matrix. We used the Sobel operator. The corresponding edge image is obtained by applying such an operator to the grey level image. After that the pixels represent the gradient instead of the grey level value. Besides that the direction vectors for each pixel are stored. This representation is calculated for the case and the actual image before the matching.

3.4. Similarity Measure based on the Dot Product.

As we have pointed out above the calculation of the Hausdorff distance is more costly than the calculation of the cross correlation. While we have to search for correspondences between case and image pixels in case of using the Hausdorff distance, we evaluate the image pixels that coincidence with the case pixels by using the cross correlation. On the other hand we are interested in matching oriented edge pixels which Olson and Huttenlocher [15] described for the Hausdorff distance. Therefore we propose a similarity measure based on the cross correlation and by using the direction vectors of an image. This approach requires the calculation of the dot product between each direction vector of the case $m_k = (v_k, w_k)^T$ and the corresponding image vector $i_k = (d_k, e_k)^T$:

$$s_1 = \frac{1}{n}\sum_{k=1}^{n} \vec{m}_k \cdot \vec{i}_k = \frac{1}{n}\sum_{k=1}^{n} \langle \vec{m}_k, \vec{i}_k \rangle = \frac{1}{n}\sum_{k=1}^{n} (v_k \cdot d_k + w_k \cdot e_k)$$

(4)

with $k = 1,\ldots,n$ case pixels.

The similarity measure of Equation (4) is influenced by the length of the vector. That means that s1 is influenced by the contrast in the image and the case. In order to remove the contrast, the direction vectors are normalized to the length one by dividing them through their gradient:

$$s_2 = \frac{1}{n}\sum_{k=1}^{n} \frac{\vec{m}_k \cdot \vec{i}_k}{\|m_k\| \cdot \|i_k\|} = \frac{1}{n}\sum_{k=1}^{n} \frac{v_k \cdot d_k + w_k \cdot e_k}{\sqrt{v_k^2 + w_k^2} \cdot \sqrt{d_k^2 + e_k^2}} \quad (5)$$

In this respect the similarity measure differs from the normalized cross correlation (NCC). The NCC normalizes each pixel value by the expected mean of all values of the considered pixels. Therefore the normalized cross correlation is sensitive to nonlinear illumination changes while our method is not because it takes only into account the angle between two corresponding direction vectors.
The values of s_2 can range from -1 to 1 . If s_2 is equal to one then all vectors in the case and the corresponding image vectors have the same direction . If s_2 is equal to -1 then all the image vectors have exactly opposite directions as the case vectors. That means that only the contrast between the case and the image is changed . T

The above described global contrast changes can be excluded by computing the absolute value of s2:

$$s_3 = \left| \frac{1}{n}\sum_{k=1}^{n} \frac{\vec{m}_k \cdot \vec{i}_k}{\|m_k\| \cdot \|i_k\|} \right| \quad (6)$$

However in case half of the vectors have the same contrast and the other half have the opposite contrast than the similarity based on s3 is zero. That might not be preferable for cases where objects are touching. To avoid this we calculate the similarity based on s4:

$$s_4 = \frac{1}{n}\sum_{k=1}^{n} \frac{\left|\vec{m}_k \cdot \vec{i}_k\right|}{\|m_k\| \cdot \|i_k\|} \quad (7)$$

4. Results

The original images (see Fig. 4a-c) are transformed into a grey level image. The thresholded image used to find the pupil and the center of mass inside the pupil is shown in Fig. 5 a-c for three subjects. Around the center of mass is set the model and then object detection is started. The edge filtered image by Sobel-phase operator is shown in Fig. 6 a-c for the three subjects. The resulting image after applying the case-based object matcher is shown in Fig. 7 a-c.

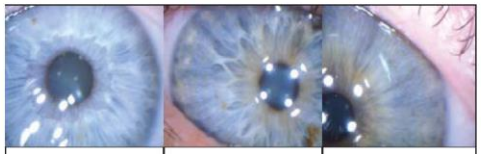

Fig. 4a Iris of Subject_1 | **Fig. 4b** Iris of Subject_2 | **Fig. 4c** Iris of Subject_3

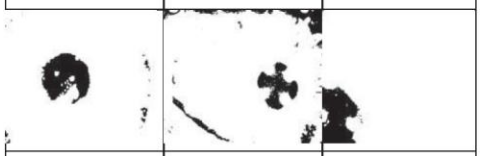

Fig. 5a Threshold image | **Fig. 5b** Threshold image | **Fig. 5c** Threshold image

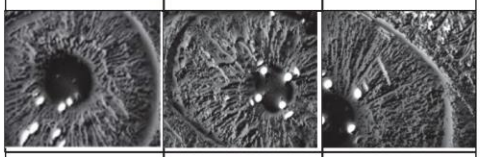

Fig. 6a Edge image | **Fig. 6b** Edge image | **Fig. 6c** Edge image

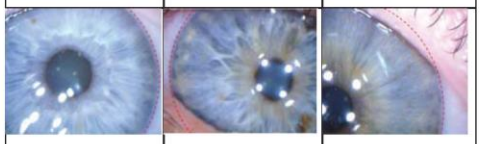

Fig. 7a Detected Iris Area | **Fig. 7b** Detected Iris Area | **Fig. 7c** Detected Iris Area

Twenty subjects participated in this study. From each of the subject were taken the iris with the handheld microscope. Four different models were inserted into the case base of the case-based matcher ranging from circular to ellipse-like model. These ellipse-like models are flattened at the bottom and the top as how it appears on the normal eye. Each of the images was preprocessed in the same way as the three images described above.

The iris could be detected by our method in all of the twenty cases. However, due to occlusion not the full iris could be seen in the image and part of the detected object needs to get removed afterwards. Since it is mostly skin and hair that occlude the iris this removal can be easily done by the color information.

5. CONCLUSION

In this paper we have presented our work on image acquisition, preprocessing and iris recognition for Iridology. We have used a handheld microscope with a ring of white lamps and equipped with a gum eye muscle in front of the microscope to acquire the iris. From the image sequence is take the image that shows most of the iris and is sharp enough for further analysis. The iris is detected with our case-based object recognition methods using different models from circular to ellipse-like models. We were able to recognize the iris of our entire subjects with good quality. Occluded areas could have been taken out based on the color information and they are not used for further evaluation. Further work will be done for image interpretation according to the knowledge of Iridology and further improvement of image acquisition.

References

[1] W. Hauser, J. Karl, R. Stolz, Iridologie 1, *Informationen aus Struktur und Farbe*, Verlag Felke Institut 2002, 260 Seiten

[2] 3. Zhongguo Yi, Liao Qi, Xie Za Zhi. The automatic iris map overlap technology in computer-aided iridiagnosis, *Chinese Journal of Medical Instrumentation*, 2002 Nov 26(6):395-7

[3] Purnomo M. et al., Iris recognition using genetic programming to detect pancreas condition related with diabetes mellitus, Proceeding *6th IASTED Intern. Conference on Visualisation, Imaging, and Image Processing,* 2006, p. 233-236

[4] Rosenberg, A. & Kagan, J., Iris pigmentation and behavioral inhibition. Developmental, (1987).*Psychobiology 20*, 377-392.
[6]7. Image understanding for iris biometrics: A survey, Computer Vision and Image Understanding 110 (2008) 281–307

[5] K. W. Bowyer, K. Hollingsworth, P. J. Flynn, Associations between the Irischaracteristics and personalities in adulthood, M. Larsson, N.L. Pedersons, H. Stattin, *Biological Psychology, Volume 75,* Issue 2, May 2007, Pages 165-175

[6] M. Larsson, Human Iris Characteristics as Biomarkers for Personality, Doctoral thesis, *Örebro University, Department of Behavioural, Social and Legal Sciences,* 2007

[7] S. El-Safadi, Komplementäre Diagnostik, Ermöglichen Irisdiagnostik / Iridologie und Dunkelfeldmikroskopie nach Enderlein die Diagnose von Malignomen? Eine prospektive Studie INAUGURAL-DISSERTATION zur Erlangung des Grades eines Doktors der Medizin *des Fachbereichs Medizin der Justus-Liebig-Universität Gießen*

[8] K. MÜNSTEDT, S. EL-SAFADI, F. BRÜCK, M. ZYGMUNT, A. HACKETHAL, and H.-R. TINNEBERG, Can Iridology Detect Susceptibility to Cancer? A Prospective Case-Controlled Study, T*HE JOURNAL OF ALTERNATIVE AND COMPLEMENTARY MEDICINE,* Volume 11, Number 3, 2005, pp. 515–519

[9] P. Perner, A. Bühring, Case-Based Object Recognition, In: Peter Funk and Pedro A. Gonzalez Calero (Eds.), Advances in Case-Based Reasoning, *Proceedings of the ECCBR 2004, Madrid/Spain, Springer Verlag 2004,* pp. 375-388

[10] P. Perner, S. Jähnichen, Case Acquisition and Case Mining for Case-Based Object Recog-nition, In: Peter Funk, Pedro A. González Calero (Eds.), Advances in Case-Based Reason-ing, Proceedings of the ECCBR 2004, Madrid/Spain, *Springer Verlag* 2004, Vol. 3155, pp. 616-629

[11] P. Perner, H. Perner, and S. Jänichen, Case-based object recognition for airborne fungi recognition, Journal Artificial *Intelligence in Medicine AIM*, Special Issue on CBR, Volume 36, Issue 2 , February 2006, p. 137-157

[12] L.G. Brown: A survey of Image Registration Techniques, *ACM Computing Survey*, Vol. 24 (4), pp. 325-376, 1992.

[13] C.F. Olson and D.P. Huttenlocher,: Automatic Target Recognition by Matching Oriented Edge Pixels, *IEEE Transactions on Image Processing*; Vol. 6 (1), pp. 103-113, 1997.

DETECTION OF CENTROBLASTS IN H&E STAINED IMAGES OF FOLLICULAR LYMPHOMA

Emmanouil Michail[1], *Evgenios N. Kornaropoulos*[1], *Kosmas Dimitropoulos*[1], *Triantafyllia Koletsa*[2], *Ioannis Kostopoulos*[2] ,*Nikos Grammalidis*[1]

[1]Information Technologies Institute, Centre for Research and Technology Hellas, Thessaloniki, Greece,
[2]Pathology Department, Medical School, Aristotle Univ. of Thessaloniki, Thessaloniki, Greece.
michem@iti.gr, ekornarop@iti.gr, dimitrop@iti.gr, koletsa@med.auth.gr, kostop@med.auth.gr, ngramm@iti.gr,

ABSTRACT

This paper presents a complete framework for automatic detection of malignant cells in microscopic images acquired from tissue biopsies of follicular lymphoma. After pre-processing to remove noise and suppress small details, images are segmented by using intensity thresholding, in order to detect the cell nuclei. Subsequently, touching cells are being separated using Expectation Maximization algorithm. Candidate centroblasts are then selected for classification by using size, shape and intensity histogram criteria. Finally, candidates are classified by using a Linear Discriminant Analysis classifier. The application of the methodology in a generated dataset of microscopic images, stained with Hematoxilin and Eosin, showed promising results by detecting in average 82.58% of the annotated malignant cells.

Index Terms— Follicular lymphoma detection, H&E stained images, centroblasts, cell segmentation, touching-cell splitting

1. INTRODUCTION

Follicular lymphoma (FL) is the second most common lymphoma diagnosed in the United States and Western Europe. It accounts for about 20% of all non-Hodgkin lymphomas [1] and mainly affects lymph nodes. When the affected lymph nodes are seen under the microscope, they show rounded structures called "follicles", which explains the term 'follicular'. The neoplastic cells consist of a mixture of centrocytes which are small- to medium-sized cells and centroblasts (CBs) which are large cells. The World Health Organization Classification has adopted grading from 1 to 3 based on the number of CBs counted per high power field (HPF) defined as 0.159 mm^2: Grade I with 0-5 CBs/HPF, Grade II with 6-15 CBs/HPF and Grade III with more than 15 CBs/HPF [1].

CB count is performed manually by the pathologist using an optical microscope and Hematoxilin and Eosin (H&E) stained tissue sections. An average CB number is calculated over ten random HPFs. Manual histological grading of FL is a time consuming process and requires considerable effort and extensive training. Furthermore, since this method uses only ten HPFs for CB count, results for specimens with high tumor heterogeneity are vulnerable to sampling bias. This may lead to inappropriate clinical decisions on timing and type of therapy [2]. Hence, there is a need for a computer assisted method which will improve reproducibility and reliability of the grading process and will reduce the time needed for diagnosis.

Computer-aided diagnosis (CAD) has been reported to be beneficial in classifying tissue subtypes associated with various grades of FL. The main steps of automatic FL grading are usually the following. The HPF image is segmented into its basic cytological components in order to extract the cell nuclei. Segmentation is usually performed using algorithms like k-means [2, 3], Expectation Maximization [4], Otsu thresholding, [5], Graph Cuts [6] etc. In many cases, segmentation algorithms tend to merge together nuclei that are too close to each other. This is usually referred to as "touching cells". Several algorithms have been proposed for touching-cell splitting, like watershed segmentation [7], radial-symmetry interest points [8], h-minima [9], active contours [10], concave points [11], ellipse/curve fitting [12], and Graph Cuts [13]. The identified cells are subsequently classified into CB and non-CB cells by extracting morphological and topological features from the cell regions [4], texture features [2, 5], as well as graph-based features [3]. Principal Component Analysis (PCA) is often employed to identify the most discriminative features.

This paper presents a complete framework for automatic CB detection in H&E stained images acquired from tissue biopsies of FL. This framework was developed to address the special characteristics of the images used in this paper. Specifically, the images were obtained from 1 to 1.5 μm thick tissue sections. The advantage of the small thickness of tissue sections is the detailed depiction of the nuclei (especially the large ones), as seen in Figure 1. Thus, contrary to microscopic images used in previous studies, nucleoli in these images are more distinguishable. However, the disadvantage is that cell segmentation and nuclei

detection is becoming difficult, since often their interior has the same color and texture as their exterior.

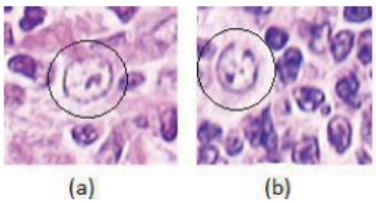

Figure 1: Details from two different HPF images, used for testing the methodology. CBs are marked with a circle.

2. METHODOLOGY

The complete image analysis scheme applied in this study is illustrated in Figure 2 and consists of five main steps: image pre-processing, image segmentation, touching-cell splitting, selection of candidate CBs and classification. These steps are described in the following subsections.

2.1 Pre-processing

The algorithm uses as input HPF images of FL stained with H&E. In order to remove noise from the image and suppress small details, input images are first converted to grayscale and filtered using a Gaussian filter with a 3x3 kernel. Additionally, in order to facilitate the detection of nuclei, differences between nuclear membrane and background are enhanced, by applying histogram equalization to the filtered image.

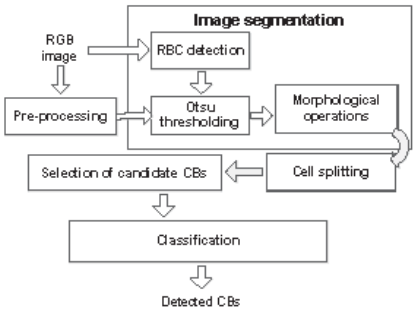

Figure 2: The logical diagram of the methodology

2.2 Image segmentation

There are five major cytological components in the FL tissue: nuclei, cytoplasm, extra-cellular material, red blood cells (RBC) and background regions [2]. Nuclei and cytoplasm regions are usually dyed with hues of blue and purple. However, in cases of large cells, nuclei also contain white components, which hinder their detection. Extra-cellular material is dyed with hues of pink and red blood cells (RBCs) are dyed with hues of red. In addition to these components, there are also white background regions that do not correspond to any tissue component.

For the identification and elimination of RBCs, an RBC mask is generated using the following threshold

$$I_{red}/(I_{red}+I_{blue}+I_{green}) > T_{RBC}$$

where I_{red}, I_{blue}, I_{green}, are pixel intensity values corresponding to red, blue and green channel respectively. The threshold is empirically set to 0.37.

After the elimination of RBC pixels, Otsu thresholding [14] is applied to the remaining pixels in the grayscale image in order to segment nuclei (dark) from extra-cellular material and background regions (bright).

As a post-processing step, connected component labelling is used to identify individual objects and an area threshold (of 10 pixels) is used to remove very small objects.

Due to the transparency of large cells[1], their interior appears hollow after Otsu thresholding. Furthermore, in some cases, the perimeter of the cells remains open after segmentation (open cells) and a simple hole-filling operation is not able to sufficiently fill the inner area of the cell. Figure 3 presents a characteristic case of an open cell. In order to address this issue, an additional post-processing procedure consisting of three steps is applied to each object in the image, which is illustrated in Figure 4. Specifically, each object is isolated and subjected to dilation with a diamond-shaped structuring element of radius r=1. Subsequently, a hole-filling operation is applied to the object and, finally, the object is subjected to erosion with the same structuring element. After this procedure, the resulting object replaces the original one in the image.

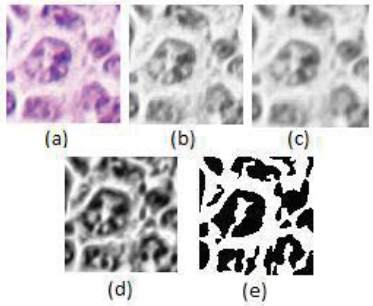

Figure 3: A detail of an HPF image containing a centroblast: a) initial image, b) grayscale image, c) image after applying Gaussian filtering, d) after histogram equalization, e) after Otsu thresholding.

[1] In the rest of the paper nuclei are also referred to as "cells"

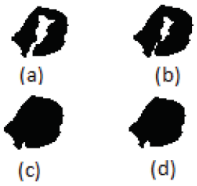

Figure 4: Post-processing procedure for open cells: a) the cell is extracted from the image, b) image dilation, c) hole-filling, d) image erosion.

2.3 Touching-cell splitting

In order to address the issue of touching-cells after segmentation, a cell-splitting algorithm is proposed based on Gaussian mixture modeling.

Initially, connected component labeling is applied and all cells larger than a threshold T_{CB} are used as candidate touching cells. T_{CB} is set to the minimum size of CBs as computed from an annotated database, consisting of CBs and non-CBs (as described in experimental results).

Expectation Maximization (EM) algorithm [15] is used to estimate a) the order of the mixture by using the minimum description length (MDL) criterion [16] and b) the parameters of the Gaussian mixture. MDL works by attempting to find the model order which minimizes the number of bits that would be required to code both the input data samples and parameters of the Gaussian mixture. Data samples consist of the pixels coordinates of each candidate touching cell; thus only spatial information is used. We observed that, when all the pixels of the cell are provided to the algorithm, MDL tends to produce a large number of clusters. Thus, subsampling is applied to the pixels according to their distance from the perimeter. An empirical threshold is set for this distance corresponding to 65% of the maximum distance. Only pixels with distance larger than this threshold are used as data samples. Despite subsampling, in some cases MDL still produces ubiquitous numbers of clusters, with their centers being too close to each other (e.g. 1 pixel). In order to address this problem, clusters that are too close to each other are being merged and the centroid of their centers is used as the center of the final cluster. The threshold for the merging is empirically set to 80% of the maximum distance from the perimeter. Figure 5 demonstrates the application of the cell-splitting algorithm on an object consisting of two touching cells.

2.4 Selection of candidate CBs

At this step candidate CB cells are being selected, based on their size, shape and intensity histogram. Initially, cells with area smaller than T_{CB} are excluded from further processing steps. Regarding the shape, we used the fact that nuclei of CB cells are usually round or oval [17]; thus cells with irregular or elongated shape are rejected. For this reason, the best fitting ellipse is estimated using the Orthogonal Distance Regression (ODR) algorithm [18]. Two criteria are used regarding the shape: a) the aspect ratio (major to minor axis ratio) and ellipse residual (average geometric distance of the pixels in the perimeter from the ellipse). Two thresholds were defined based on the annotated CB training set. The thresholds for aspect ratio and ellipse residual were set to 2.8 and 1.8 respectively. Cells with values larger than these thresholds are discarded. In order to exclude some small dark non-CB cells, the mean value of the grayscale histogram was computed over the CB training set and a threshold was set to 135.7. Cells with mean histogram value smaller than this threshold are excluded. All remaining cells are provided to the classification step as candidate CBs.

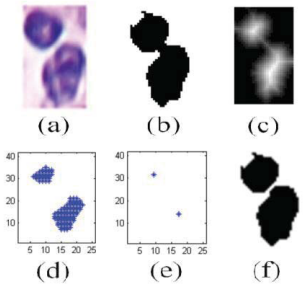

Figure 5 Cell splitting on touching cells: a) initial image, b) image after segmentation, c) the Euclidean distance of each pixel from the perimeter, d) the most distant pixels from the perimeter, e) the centers of connected cells, as computed by the MDL, f) splitted cells according to the result of EM.

2.5 Classification

For the classification between CBs and non-CBs, the annotated database of CBs and non-CBs was used as a training set. An *mxn* matrix A was defined having as elements the intensity values of all images of the training set, where n is the total number of training images (CBs and non-CBs) and m is the number of pixels in each image (in our experiments: 71x71).

$$A = \begin{bmatrix} p_{11} & \cdots & p_{n1} \\ \vdots & \ddots & \vdots \\ p_{1m} & \cdots & p_{nm} \end{bmatrix}$$

Then, in order to remove the redundancy from the image set, Singular Value Decomposition (SVD) is used. According to SVD, A can be written as:

$$A = U \begin{pmatrix} \Sigma \\ 0 \end{pmatrix} V^T$$

where U is an *mxm* matrix and V is a *nxn* matrix, representing the left and right eigenvectors of A respectively. Moreover, Σ corresponds to the eigenvalues of A. The left eigenvectors are an orthogonal basis for the column space of A, i.e. the "image space of CBs and non-

CBs". The eigenvector with the highest eigenvalue points to the highest variance among the images. We assume that the discriminative features of CBs/non-CBs will be revealed on the directions pointing to the highest variance among the images. Therefore, eigenvectors are ordered in a sequence of descending eigenvalues. The projection of training images onto a subspace which spans by only the first few eigenvectors will well characterize the cells. In our case 47 eigenvectors were used, which was the optimal number as indicated by the training results of the classifier.

Each candidate CB in the testing image is subjected to classification according to the following procedure: The centroid of the cell is computed and a 71x71 region of the initial image is kept around this centroid. The projected training and testing images are used as input to a Linear Discriminant Analysis (LDA) classifier, in order to classify them into one of two classes (CBs and non-CBs).

In order to compute the optimum number of eigenvectors, that would reveal the most discriminative features of CB and non-CB images, we trained the classifier based on "Hold-out K-folds" cross-validation approach [19]. For this reason, the images of CBs and non-CBs were randomly divided K times into training (80%) and validation (20%) set. The training set was further processed in order to obtain the optimal number of eigenvectors. Specifically, after examining every number of eigenvectors from 1 to 50, the optimal number of eigenvectors was selected to be the smallest one through which the best classification results were calculated. After computing the optimal number of eigenvectors at each of the K iterations, classifier's accuracy was validated by using the validation set, and the final optimal number of eigenvectors was regarded as the one derived by the iteration that produced the best classification results. Empirically, K was set to 10.

3. EXPERIMENTAL RESULTS

The methodology described in previous section was tested on three 40× microscopic HPF images derived from tissue biopsies of grade II FL, stained with H&E. Images were acquired at the Pathology Department of Medical School of Aristotle University of Thessaloniki, Greece. Tissue sections were sliced at a thickness of 1 to 1.5. They were scanned using Nikon DN100 digital network camera and were inspected by two medical experts, in order to identify the number of CBs in each image. The average number of CBs in each image was 10.

In addition, a training set containing cropped images of CBs and non-CBs was generated for the classification process. Specifically, nine HPF images of FL, stained with H&E, were scanned by using the same procedure as for the testing images. Subsequently, they were examined by medical experts in order to mark CBs on them. By using these markings, a set of cropped images of CB cells was created. Each cropped image contains the CB cell at its center and is of size 71x71 pixels. Similarly, a second set of images of size 71x71 pixels containing only non-CBs was created. In total, a training set of 70 images of CBs and 110 images of non-CBs was used.

The overall efficiency of the algorithm was assessed by comparing CBs that were annotated by doctors with the detected CBs. 82.58% of the annotated CBs were successfully detected on average in the three images. The disadvantage of the methodology is that it produces a large number of false positives. Specifically, the average number of false positives in the three images was 50. Analytical results are shown in Table I.

TABLE I. IMAGE ANALYSIS RESULTS

	Image 1	Image 2	Image 3	Average
Annotated CBs	11	8	11	10
Detected CBs	52	55	68	5
True positives	10	6	9	8,3
False negatives	1	2	2	1.6
False positives	42	49	59	50
Correct detection rate[a]	90%	75%	81%	82.52%

[a] Number of TPs divided by the number of annotated CBs.

The large number of false positives might be partially explained by the resemblance of certain types of large cells, like endothelial and dendritic cells to CBs. As already mentioned, the transparency of large cells poses a problem on the detection of nuclei, but also provides a better description of the nuclear area. In this paper the effort was focused mainly on the accurate extraction of cells. Future work should focus on the development of a texture descriptor that will detect differences between the different kinds of large cells.

4. CONCLUSIONS AND FUTURE WORK

A complete methodology was proposed in this paper for detection of CBs in H&E stained microscopic images of FL. The methodology addresses the special characteristics of the images used and specifically, the transparency of the nuclei due to the small thickness of tissue sections. Intensity thresholding has been used for the segmentation of images into their cytological components. Additionally, Expectation Maximization algorithm is being used for the separation of touching cells. Candidate CBs are selected by using size, shape and intensity histogram criteria. Finally, candidates are classified into CBs and non-CBs by using a Linear Discriminant Analysis classifier. An average number of 82.58% of the annotated CBs was detected in three HPF images. However, the algorithm also produces a large number of false positives and future work should focus on their elimination by investigating textural differences between CBs and large non-CB cells.

5. REFERENCES

[1] A. Freedman, "Follicular Lymphoma: 2012 Update on Diagnosis and Management," *Am. J. Hematol.*, vol. 87 (10), pp. 988-995, 2012.

[2] O. Sertel, J. Kong, and Ü. V. Çatalyürek, G. Lozanski, J. H. Saltz, M. N. Gurcan, "Histopathological Image Analysis Using Model-Based Intermediate Representations and Color Texture: Follicular Lymphoma Grading," *Signal Processing Systems*, vol. 55 (1-3), pp 169-183, 2009.

[3] B. Oztan, H. Kong, M. Gurcan, and B. Yener, "Follicular Lympoma Grading using Cell-Graphs and Multi-Scale Feature Analysis," *Proc. SPIE Medical Imaging*, San Diego, USA, 2012.

[4] O. Seterl, G. Lozanski, A. Shana'ah, M. Gurcan, "Computer-Aided Detection of Centroblasts for Follicular Lymphoma Grading Using Adaptive Likelihood-Based Cell Segmentation," *IEEE Trans. Biomed. Eng.*, vol. 57 (10), 2010.

[5] K. Belkacem-Boussaid, O. Sertel, G. Lozanski, A. Ahana'aah,and M. Gurcan, "Extraction of Color Features in the Spectral Domain to Recognize Centroblasts in Histopathology," *Conf. Proc. IEEE Eng. Med. Biol. Soc.*; Minneapolis, USA, 2009.

[6] Y. Boykov, and M-P. Jolly. "Interactive Graph Cuts for Optimal Boundary and Region Segmentation of Objects in N-D Images," *Proceedings of IEEE International Conference on Computer Vision,*, vol. 1, pp. 105-112, 2001.

[7] V. Grau,, A. U. Mewes M. Alcaniz, R. Kikinis, and S. K. Warfield, "Improved Watershed Transform for Medical Image Segmentation Using Prior Information," *IEEE Trans. Med. Imaging*, vol. 23 (4), pp. 447-458, 2004.

[8] H. Kong, M. Gurcan, and K. Belkacem-Boussaid, "Partitioning Histopathological Images: an Integrated Framework for Supervised Color-texture Segmentation and Cell Splitting," *IEEE Trans. Med. Imaging*, vol. 30(9), pp. 1661-1677, 2011.

[9] P. Soille, *Morphological Image Analysis: Principles and Applications*, Springer-Verlag, Berlin, Germany, 1999.

[10] J. Cheng, and J. Rajapakse, "Segmentation of Clustered Nuclei with Shape Markers and Marking Function,"*IEEE Trans. Biomed. Eng.*, vol. 56 (3), pp. 741-748, 2009.

[11] L. Yang, O. Tuzel, P. Meer, and D.J. Foran, "Automatic Image Analysis of Histopathology Specimens Using Concave Vertex Graph," *Med. Image Comput. Comput. Assist. Interv.*, , vol. 1, pp. 833-841, 2008.

[12] C. Cong, and B. Parvin, "Model Based Segmentation of Nuclei," *IEEE International Confernce on Computer Vision and Pattern Recognition*,vol. 1, 1999.

[13] Y. Al-Kofahi, W. Lassoued, W. Lee, and B. Roysam, "Improved Automatic Detection and Segmentation of Cell Nuclei in Histopathology Images,"*IEEE Trans. on Biom. Eng.*," vol. 57 (4), pp. 841-852, 2009.

[14] N. Otsu, "A Threshold Selection Method from Gray-level Histograms," *IEEE Trans. Sys. Man. Cyber.*, vol9, pp. 62-66, 1979.

[15] C. A. Bouman, "Cluster: An unsupervised algorithm for modeling Gaussian mixtures," Available from https://engineering.purdue.edu/~bouman/software/cluster/cluster-matlab/, September 2013.

[16] J. Rissanen, "A Universal Prior for Integers and Estimation by Minimum Description Length," *Annals of Statistics*, vol. 11 (2), pp. 417-431, 1983.

[17] E. S. Jaffe, N. L. Harris, J. Vardiman, E. Campo, and Daniel MD Arber, *Hematopathology*, Elsevier Health Sciences, Philadelphia, USA, 2010.

[21] W. Gander, G. H. Golub, and R. Strebel, "Least-square fitting of circles and ellipses," *BIT*, vol. 43, pp. 558-578, 1994.

[22] S. Arlot, and A. Celisse, "A survey of cross-validation procedures for model selection," *Statistics Survey*, vol. (4), pp. 40-79, 2010.

Photos from Workshop

Figure 2 MIRACLE Participants

Figure 3 Presentations


Figure 4 Plenary Speakers